Proposal Code CH-5458

Confidential experimental report: this paper will be submitted in April 2021

Out-of-equilibrium decoupling of volume and ferroelastic lattice strains driven by the self-trapping of photo-induced charge-transfer in a Prussian Blue Analogue

Giovanni Azzolina,[a] Eric Collet,*[a] Céline Mariette,[a] Marco Cammarata,[a] Elzbieta Trzop,[a] Herve Cailleau,[a] Claude Ecolivet,[a] Mathias Sander,[b] Matteo Levantino,[b] Hiroko Tokoro,[c] Shin-ichi Ohkoshi,[d] Roman Bertoni*[a]

[a] Univ Rennes, CNRS, IPR (Institut de Physique de Rennes) - UMR 6251, F-35000 Rennes, France

[b] European Synchrotron Radiation Facility, F-38000 Grenoble, France.

[c] Department of Materials Science, Faculty of Pure and Applied Sciences, Univ Tsukuba, 1-1-1 Tennodai, Tsukuba, Ibaraki 305-8577, Japan.

[d] Department of Chemistry, School of Science, The University of Tokyo, 7-3-1 Hongo, Bunkyo-ku, Tokyo 113-0033, Japan.

E-mail: roman.bertoni@univ-rennes1.fr, eric.collet@univ-rennes1.fr

Abstract 150 words: Photo-induced structural dynamics in molecular materials often involve two main components; local molecular distortions induced by the self-trapping of electronic excited state and incoherent lattice dynamics due to energy dissipation. The latter component frequently hinders clear manifestation at macroscopic scale of local self-trapped entities and their coupling to the lattice. The studied material RbMnFe is a Prussian Blue Analogue that exhibits no thermal expansion, which allows for the observation of long-range dynamics induced by the structural trapping of photoinduced charge-transfer states. Indeed the photoinduced $Mn^{III}Fe^{II}$ to $Mn^{II}Fe^{III}$ charge-transfer states correspond to small-polarons, involving local Jahn-Teller distortion and volume expansion, responsible for the emergence of various physical properties. At equilibrium, the lattice expansion and the ferroelastic Jahn-Teller distortion evolve in a coupled way. Here, we use time resolved X-ray diffraction to investigate the anisotropic out-of-equilibrium lattice dynamics triggered by the self-trapping of CT state induced by ultrafast optical excitation. The observed dynamics evidence a decoupling of both types of lattice deformation in the time domain, with an impulsive lattice response due to Jahn-Teller reorganization and displacive volume expansion controlled by the long-lived fraction of self-trapped photo-induced CT state.

Introduction

Ultrafast photo-induced dynamics in materials results from complex couplings between electronic and structural reorganizations, responsible amongst other things for the stabilization of photo-induced orders.[1-4] The initial electronic excited state may involve strongly dispersive states, reaching quickly new thermal distribution, which can drive structural motion within the unit cell and later on global lattice expansion.[5-7] In molecular materials with weakly dispersive electronic states, the initial excitation can be structurally trapped at the molecular level, precluding fast decays of excited electronic state.[4, 8, 9] Often in time-resolved experiment, it is difficult to discriminate the contribution of local structural distortions induced by electronic excited states from the lattice dynamics generated by the incoherent population of phonons. Therefore, materials presenting structural distortion without thermal expansion are ideal playground to investigate interactions of quasi-particles such as self-trapped small-polarons with the lattice,[10, 11] which may trigger long-range lattice deformations in materials.[12-16]

Cyano-bridged bimetallic systems are of specific interest, since they exhibit various types of orders tunable by light, like reversible ferro- or antiferro-magnetism. Those functions are based on photo-induced intermetallic charge transfer (CT) or spin-transition (ST) coupled to structural self-trapping and symmetry changes.[17-22] Prussian blue analogues (PBA) in particular are characterized by CT based transformation that are strongly cooperative due to the important volume change accompanying both thermal and steady photo-induced phase transition,[23-25] and which implies strong interactions of the CT process with the lattice. It is therefore compulsory to understand the coupling between self-trapped CT excitation, known as small-polarons,[26] and the lattice and its impact in the emergence of macroscopic order and functionalities.

Here we study the photo-induced out-of-equilibrium dynamics in the RbMnFe PBA system,[27-29] which undergoes a CT-based phase transition resulting from the coupling between intermetallic CT, responsible for an important non-symmetry-breaking volume (*V*) strain, and a symmetry-breaking Jahn-Teller distortion associated with ferroelastic shear strain η. In the framework of the Landau theory of phase transitions, we have shown that due to their elastic coupling, *V* and η change simultaneously at thermal equilibrium during the CT-based phase transition.[30] Here we investigate the lattice dynamics resulting from the photoinduced Fe-to-Mn CT process by time-resolved X-ray diffraction,[4, 31, 32] which allows for monitoring in real time the long-range lattice reorganization. The observed dynamics reveal the decoupling in the time domain of the non-symmetry-breaking (nsb) volume strain and symmetry-breaking (sb) ferroelastic strain. We show that the fraction of less-bonding self-trapped CT excited state, controlled by light excitation, acts as an external parameter for lattice expansion, allowing for reaching a transient state hidden at thermal equilibrium.

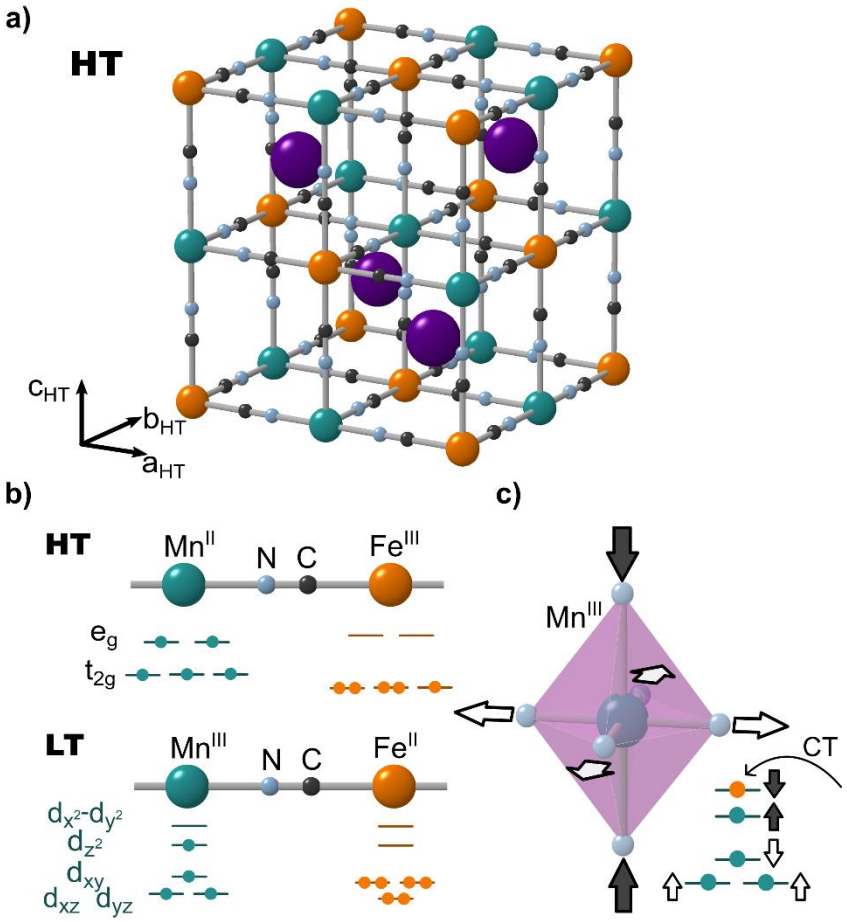

Figure 1: (a) Structure of RbMnFe system in the cubic HT phase. Mn, N, C, Fe and Rb are shown in green, light blue, black, orange and purple respectively. (b) Schematic valence states and electronic configurations in the LT $Mn^{III}Fe^{II}$ and HT $Mn^{II}Fe^{III}$ phases. (c) The $Mn^{III}Fe^{II}$ to $Mn^{II}Fe^{III}$ charge transfer is stabilized by the reverse Jahn-Teller distortion as the Mn $d_{x^2-y^2}$ is populated.

We studied the RbMnFe system (Fig. S1), with composition $Rb_{0.94}Mn[Fe(CN)_6]_{0.98}\cdot 2.5H_2O$, which exhibits bistability between two phases with different structural and electronic configurations (Fig. 1a,1b). The high temperature (HT) phase forms a FCC lattice with metals in O_h ligand fields of electronic configuration Mn^{II}(S=5/2)Fe^{III}(S=½). The low temperature (LT) phase is tetragonal, as a Jahn-Teller distortion stabilizes the Mn^{III}(S=2)Fe^{II}(S=0) electronic configuration (Fig. 1b).[30] Various techniques described the occurrence of the CT-based phase transition from $Mn^{III}Fe^{II}$ (LT) to $Mn^{II}Fe^{III}$ (HT) at thermal equilibrium, or under continuous light irradiation at low temperature.[19, 33-35] The degree of CT is monitored through the evolution of the totally symmetric order parameter γ, measuring the fraction of $Mn^{II}Fe^{III}$ CT state that changes from γ=0 in the LT phase to γ=1 in the HT phase. γ is usually probed by magnetism or optical spectroscopies.[34, 36] The thermal phase transition exhibits a wide hysteresis[37] (T_{up}≈285K, T_{down}≈185 K) as revealed by magnetic susceptibility (Fig. S2). Fig 2a shows the important changes in the lattice parameters on warming from the LT tetragonal space group $F\bar{4}2m$ ($\boldsymbol{a}_{LT}$=10.059(3) Å, $\boldsymbol{c}_{LT}$=10.502(3) Å) to the HT cubic space group ($F\bar{4}3m$, $\boldsymbol{a}_{HT}$=10.563(1) Å). Our X-ray diffraction data (Fig. 2d) highlight the symmetry change during the CT-based phase transition, with a zoom in the ranges of scattering vector $\boldsymbol{q}$ [1.13-1.31 $Å^{-1}$] and [2.29-2.61 $Å^{-1}$]. The (h00) and (00l) peaks are equivalent in the cubic HT phase and correspond to the same $\boldsymbol{q}$. In the LT tetragonal phase the (h00) and (00l) peaks split and correspond to different $\boldsymbol{q}$, due to the stronger contraction along $\boldsymbol{a}$ compared to $\boldsymbol{c}$. As explained recently,[30] this structural instability occurs at the Γ point of the Brillouin Zone and the transition can be described at equilibrium in terms of two coupled order parameters.

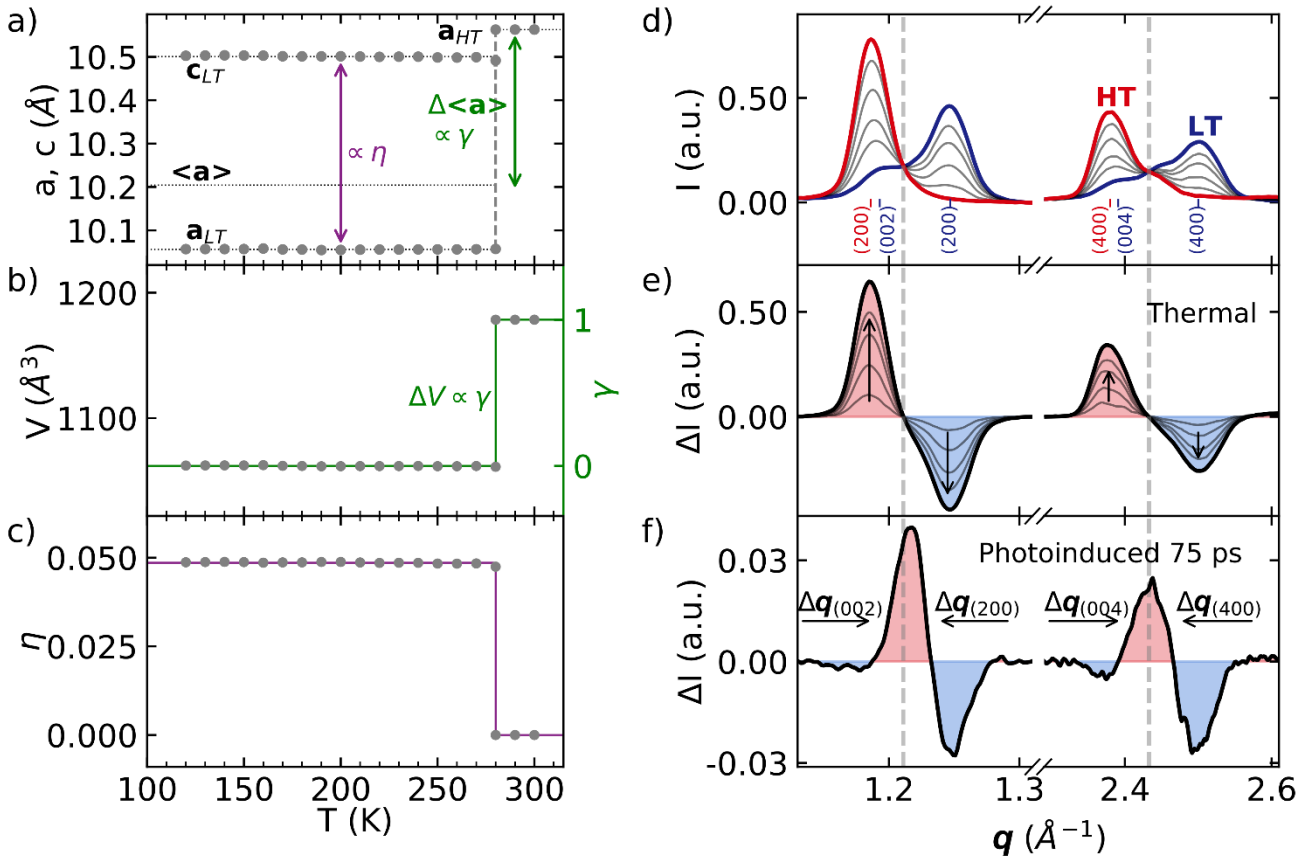

*Figure 2: (a) Lattice parameters upon warming. The solid lines mark the average values in each phase. The dotted line marks the beginning of the ascending branch of the hysteresis from LT to HT phases. The vertical and thick arrows refer to non-symmetry-breaking (γ, green) and symmetry breaking (η, purple) changes. (b) Thermal evolution of the lattice volume, scaled in CT fraction γ(T) (right axis). (c) Thermal evolution of the amplitude η of the symmetry breaking. (d) Evolution of the powder diffraction patterns along the scattering vector **q** from LT (blue) to HT (red) phases, zoomed in the [1.13-1.31 Å^{-1}] and [2.29-2.61 Å^{-1}] ranges. The grey lines show intermediate temperature between LT and HT phases. (e) Temperature evolution of the differential X-ray diffraction signal with respect to 120 K (LT). (f) Time-resolved differential X-ray diffraction signal, with respect to negative delay, measured 75 ps after photoexcitation.*

The ferroelastic cubic-tetragonal distortion is the symmetry-breaking (sb) order parameter, which belongs to the E representation of the HT $\bar{4}3m$ point group.[30] Fig. 2c shows its amplitude defined as $\eta(T) = \frac{2}{\sqrt{3}}(\frac{c(T)-a(T)}{a_{HT}})$. This anisotropic distortion obeys transformation properties ($2z^2$-x^2-y^2) of the Jahn-Teller mode[30] elongating ***c*** and contracting the other axes ***a*** = ***b*** and results in a splitting of the lattice parameters in the LT phase:

$$\boldsymbol{\Delta a_{sb}} = \frac{1}{2}(2\boldsymbol{a_{LT}} - \boldsymbol{a_{LT}} - \boldsymbol{b_{LT}}) = \boldsymbol{c_{LT}} - \boldsymbol{a_{LT}} = 0.443(1)\ \text{Å}.$$

The non-symmetry-breaking (nsb) volume strain is related to the average change of the lattice parameter:

$$\boldsymbol{\Delta a_{nsb}} = \boldsymbol{a_{HT}} - < \boldsymbol{a_{LT}} > = 0.353(1)\ \text{Å}, \text{ with } < \boldsymbol{a_{LT}} > = \frac{1}{3}(2\boldsymbol{a} + \boldsymbol{c}) = 10.204(1)\ \text{Å}.$$

Indeed, during the LT to HT phase transition, the population of the anti-bonding Mn dx^2-y^2 state in the $Mn^{II}Fe^{III}$ HT phase favors O_h symmetry around the manganese, reorganizing so the energy levels of the orbitals.[34] The LT

Mn-N bonds along *x* and *y* (≈1.89 Å) expand and the ones along *z* (≈2.29 Å) shorten (Fig. 1c) to get equivalent (≈2.05 Å) in the cubic HT phase.[38-42] Due to the polymeric nature of the lattice, and the additional elongation of the Fe-C bonds, the CT transition from the $Mn^{III}Fe^{II}$ LT towards the less-bonding $Mn^{II}Fe^{III}$ HT phases results in a global volume expansion from V_{LT}=1062.2(2) Å^3 to V_{HT}=1178.5(2) Å^3 (Fig. 2b). This large volume change is responsible for the phase nucleation process, where the HT and LT phases coexist, which translates into a weight transfer between HT to LT Bragg peaks during the transition (Fig. 2d, 2e). In the frame of the Landau theory of phase transition,[30] we have shown that the volume change at the transition is linearly coupled to the totally symmetric order parameter γ, which is the main contribution to volume expansion.[30, 43] Since this system exhibits zero thermal expansion in LT or HT phases[23] and the volume changes from V_{LT} in the LT phase (γ=0) to V_{HT} in the HT phase (γ=1), the thermal evolution of the fraction of $Mn^{II}Fe^{III}$ CT state $\gamma(T)$ can then be derived from the relative lattice expansion with respect to the LT phase:

$$\gamma(T) = \frac{V(T)-V_{LT}}{V_{HT}-V_{LT}}$$

shown in Fig. 2b (right axis). Our recent study explained that, at thermal equilibrium, the simultaneous and discontinuous change of the parameters monitoring the CT (γ and *V*) and the ferroelastic symmetry breaking (η), is due to their elastic coupling.[30]

In addition to thermal equilibrium phase transition, the CT between the ground $Mn^{III}Fe^{II}$ and $Mn^{II}Fe^{III}$ configurations can also be photo-induced.[27, 28] Nevertheless, the dynamics resulting from the interaction of the local structural self-trapping process of this photoinduced CT with the surrounding lattice is currently unknown,[19, 33] as the techniques used so far were lacking time resolution. Hereafter, we use ultrafast time-resolved x-ray diffraction to study the lattice response to a laser pulse, driving the photoinduced CT. The ultrafast photo-induced lattice dynamics is monitored with optical pump — X-ray probe configuration at the ERSF ID09 beamline[44] with ~70 ps experimental time resolution (supplementary information). The sample is cool down at 110, 130 and 160 K in the LT phase $Mn^{III}Fe^{II}$ and excited with 1 ps laser pulses centered at 520 nm. This optical excitation is known for promoting the intervalence electron transfer from Fe to Mn to create the $Mn^{II}Fe^{III}$ configuration.[19, 27, 28] The ≈300 nm typical size of the nanocrystals (Fig. S1),[23] similar to the pump penetration depth (≈350 nm),[29] ensures a rather homogeneous excitation at the individual nanocrystal scale. The photo-induced CT process occurs on the picosecond time scale and the resulting transient electronic state lasts for more than 10 µs, as revealed by different techniques.[45, 46]

Results

Fig. 3a & 3b display the evolution of lattice parameters at 130 K, normalized to their values before photoexcitation, for two excitation densities and more data are shown in Fig. S5. Fig. 3c & 3d show the temporal evolutions of the normalized lattice volume *V* and ferroelastic distortion η. The data highlight the presence of the two distinct steps in the out-of-equilibrium lattice dynamics. Immediately after laser excitation the lattice parameter ***a*** increases, while ***c*** decreases simultaneously, and both reach extrema within the experimental time resolution. The relative diffracted intensity difference between 75 ps and negative delay (Fig. 2f) shows this

anisotropic lattice response. It is characterized by a shift of the (00l) Bragg peaks towards higher scattering vector ***q***, corresponding to the contraction of the ***c*** axis (Fig. 3b), and the opposite shift of the (h00) peaks towards lower ***q***, corresponding to the expansion of the ***a*** axis (***a***=***b*** Fig. 3a). This is strikingly different from the simultaneous expansion of ***a*** and ***c*** observed during the thermal equilibrium transition (Fig. 2e), where (h00) and (00l) low temperature peaks become equivalent in the cubic HT phase. However, 75 ps after photoexcitation the increase of V and decrease of η moves the system towards the values of the HT phase.

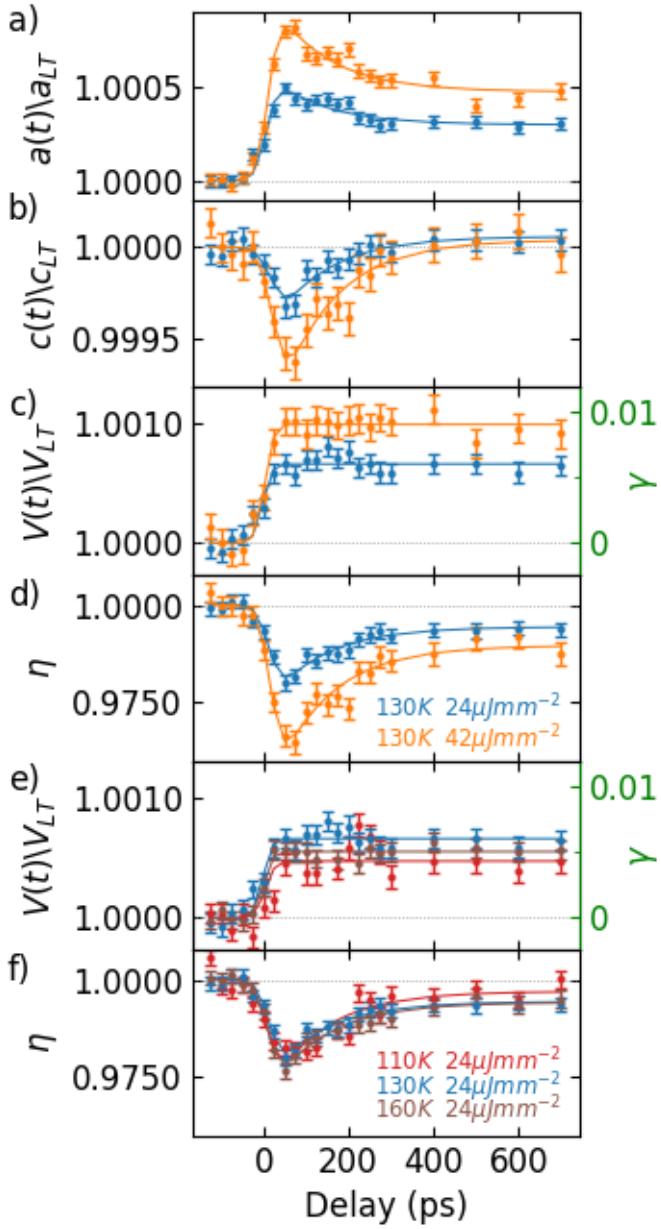

*Figure 3: (a, b, c, d) Relative temporal evolution of the lattice parameters **a**, **c**, V* and *η, with respect to values prior to photoexcitation at 130 K, for pump fluences of 24 µJ.mm^{-2} (blue) and 42 µJ.mm^{-2} (orange). The solid lines represents the fit of the data. (e) and (f) show the relative evolution of V and η at 110 K, 130K and 160 K.*

In a second step, the partial decrease of ***a*** is accompanied by an increase of ***c***, which recovers values almost similar to the ones prior to optical excitation. Compared to negative delay, the relative diffracted intensity

changes at 600 ps shown in Fig. S8, corresponds mainly to a shift towards lower ***q*** of the (h00) peaks, i.e. an expansion along the ***a*** axis. This different evolution of ***a*** and ***c*** increases the ferroelastic distortion η, which recovers values close to initial equilibrium conditions. However, the lattice volume *V* remains constant after photoexcitation and larger than at equilibrium (Fig. 3c & 3d). For describing the ultrafast volume expansion, occurring within the time resolution, we used a step function convoluted with the instrumental response function (Fig. 3c, 3e and S6). An additional exponential relaxation (τ_r=130 ps) provides a satisfactory guide for the eye to describe the decay in (Figs 3a, 3b, 3d, 3f and S6). The initial expansion of ***a*** and contraction of ***c*** are also quite linear with excitation densities (Fig. S7). In addition, the photo-responses, at 110 and 160 K are similar to the ones at 130 K for similar excitation densities (Fig. 3e-f).

Photo-induced phase transitions are intricate with the concept of cooperative and non-linear response to light perturbation, allowing for the emergence of long-range structural and electronic orders.[8, 32, 47, 48] However, cumulative changes within the kHz repetition rate of the experiment precluded investigations with excitation above ≈ 42 μJ.mm^{-2}. In the excitation density regime explored here, we did not observe any cooperative phenomena like partial formation of cubic phase, neither non-linear photo-response. We focus then our attention on the dynamics of precursor phenomena driven by photoinduced self-trapped CT states.

Discussion

We should underline that, since this system exhibits no thermal expansion,[23, 30] the observed volume expansion is not due to laser heating, through the incoherent lattice phonon population. The photo-responses are also similar in shapes or amplitudes, for different excitation densities and over a wide temperature range (110-160 K), well below the phase transition temperature (300 K), which confirms the non-thermal origin of the response. The absence of excitation densities dependence in the lattice response timescale, the linear response to excitation density (Figure S7) and the anisotropic structural dynamics suggest that the origin of this macroscopic long-range lattice dynamics is the local self-trapping of the photoinduced CT. Indeed, previous experiments have shown that photoexcitation of the $Mn^{III}Fe^{II}$ state drives the intervalence electron transfer to create the $Mn^{II}Fe^{III}$ configuration.[19, 34] The associated population of Mn dx^2-y^2 state (Fig. 1c) is stabilized by elongating the Mn-N bonds along *x* and *y*, which reduces the Jahn-Teller distortion and brings the Mn sites towards O_h symmetry.[34] Time-resolved infrared spectroscopy evidenced that this local lattice deformation, dissolving the Jahn-Teller distortion, occurs within ≈1 ps.[46] In a similar CoFe analogue, femtosecond XANES experiments monitored the Co-N bond elongation, trapping the photoinduced CT, within 50 fs.[22]

This anisotropic structural self-trapping of the $Mn^{II}Fe^{III}$ CT state results in a local lattice distortion, characteristic of these small-polarons,[26, 34] elastically coupled to the lattice. These local and reverse Jahn-Teller distortions around the MnN_6 octahedron, within the cyano-bridged polymeric lattice, generate anisotropic strains, sources of elastic deformation waves travelling through the crystals.[8] The structural trappings of the CT states within the crystal, elongating Mn-N bonds along *x* and *y* and contracting those along *z*, result then in a global expansion of ***a*** and ***b*** axes and a contraction of the ***c*** axis (Fig. 4a). Such elastic deformations propagate typically with sound velocity (c = 4300 m/s)[49] and the characteristic timescale τ_{ED} for volume expansion scales to the average crystal

size[8] ($r \approx 3.10^{-7}$ m). $\tau_{ED} = \frac{r}{c} \approx 70\ ps$ falls within our time resolution. The anisotropic structural reorganization around the self-trapped CT state, dissolving the Jahn-Teller distortion, is responsible for the initial decrease of the ferroelastic distortion η, while its less bonding nature accounts for the global volume increase.

After this initial structural dynamics, the volume strain and the ferroelastic distortion decouple in time. The photo-induced CT $Mn^{II}Fe^{III}$ state is long-lived due to the structural trapping, as previously observed by optical and X-ray spectroscopy.[45] Fig. S9 shows that volume relaxation occurs within 10s µs, which corresponds to the lifetime of the self-trapped CT state as monitored by optical density.[45] Given that the fraction $\gamma^{h\nu}$ of photoinduced CT states couples linearly to the volume strain,[30] that these live much longer than the elastic equilibration timescale of the lattice and that there is no thermal lattice expansion in this system, the lattice expansion directly correlates to $\gamma^{h\nu}$ and both are transiently locked up after photoexcitation. The observed 0.1% volume change after photoexcitation, compared to the 10% volume change when CT is complete during the thermal transition, provides a rough estimate of $\gamma^{h\nu}$ =1% (Fig. S7), which confirms the local nature of the process. In order to restore elastic equilibrium, the internal stress due to long-range structural deformations related to the formation of CT small-polarons must be minimized. The ferroelastic deformation η, initially reduced by local distortions, has to equilibrate with the globally tetragonal lattice surrounding the small-polarons, and it almost recovers the equilibrium value within ≈500 ps. On contrary, the long lifetime of the self-trapped CT state, of higher molecular volume, prevents lattice contraction and locks transiently the crystalline volume over 10s µs (Fig. S9). The volume strain and the ferroelastic distortion decouple then in time because different processes drive their dynamics. The volume expansion corresponds to a displacive process, driven by the long-lived fraction $\gamma^{h\nu}$ of photoinduced $Mn^{II}Fe^{III}$ sites of higher volume. The evolution of η is mainly impulsive as characterized by its initial overshoot, in response to local and anisotropic distortions. Indeed, due to anisotropy the effect of the local and reverse Jahn-Teller reorganizations superpose and drive anisotropic lattice response. This decoupling in the time domain of the ferroelastic deformation and volume strain differs from thermal equilibrium transformation, where *V* and η change in a coupled way. The transient photoinduced lattice parameters after 500 ps corresponds then to a transient state, not observed at thermal equilibrium.

Fig. 4b shows a schematic evolution of the potential at equilibrium, with a single equilibrium volume V_{LT} or V_{HT}, except in the hysteresis region where both coexist. The zero thermal expansion in the investigated temperature range[23] implies a quasi-harmonic potential around V_{LT} and V_{HT}. The evolution of the partial DOS on the Mn after photoexcitation (Fig. 4c) qualitatively explains the observed dynamics, as the lattice potential is modified by the fraction of CT state $\gamma^{h\nu}$. This partial population of antibonding Mn dx^2-y^2 states launches the reverse Jahn-teller distortion and results in a self-trapping of the CT state (Fig. 1c). The Mn-N bonds elongate then along *x* and *y*, which expands the ***a*** and ***b*** lattice axes, shifting so the transient equilibrium volume of the photoexcited state compared to the ground state (Fig. 4a). Since the photo-excited state leaves 10s µs, the lattice has to accommodate to the photoinduced population of antibonding electronic states. $\gamma^{h\nu}$ plays therefore the role of an external parameter controlled by light and acting on the lattice volume.

Conclusion

Thanks to the ideal playground offered by the RbMnFe material, it is possible to investigate the interaction of structurally self-trapped CT excited states with the lattice, without parasitic contribution from incoherent phonon population. The observed dynamics is rationalized in terms of anisotropic lattice deformations related to symmetry breaking ferroelastic distortion (η) and non-symmetry-breaking volume expansion (V), which are driven by the self-trapping of photoinduced CT states. Contrary to the case of delocalized electronic excitation,[50] which rapidly thermalize with the lattice, the out-of-equilibrium electronic distribution of excited CT state is not relaxing to the electronic ground state. Indeed, the local and anisotropic structural reorganization of the Mn-N bonds, elongating by ≈10 %, results in the formation of small-polarons.[26, 34] This prevents fast decay towards the ground state of the less bonding electronic excited state. The lattice deformations driven by those local self-trapped CT states superpose in a constructive way due to anisotropy, which launches a long-range lattice dynamics. The initial impulsive response driven by the anisotropic strain induced by the local self-trapping corresponds to a displacive process, shifting the macroscopic crystal volume. Within ~500 ps after photoexcitation, the ferroelastic distortion relaxes to minimize the global elastic cost, while the long-lived CT small-polarons prevents fast volume relaxation. The high sensitivity of the technique and the large and anisotropic local distortions allow for analyzing how local precursor phenomenon couple to the lattice. The present study highlights that describing the self-trapping dynamics at the scale of the photoactive site only is not sufficient in solid state. Indeed, the elastic energy of the lattice has to be considered in the out-of-equilibrium process, as it is the case at thermal equilibrium in volume-changing molecular magnetic materials.[51] Our results highlight the strong interactions of self-trapped photoinduced state with the lattice, which is often neglected, that may play a key role in the inhibition or amplification of photo-induced transformations in volume-changing molecular systems.

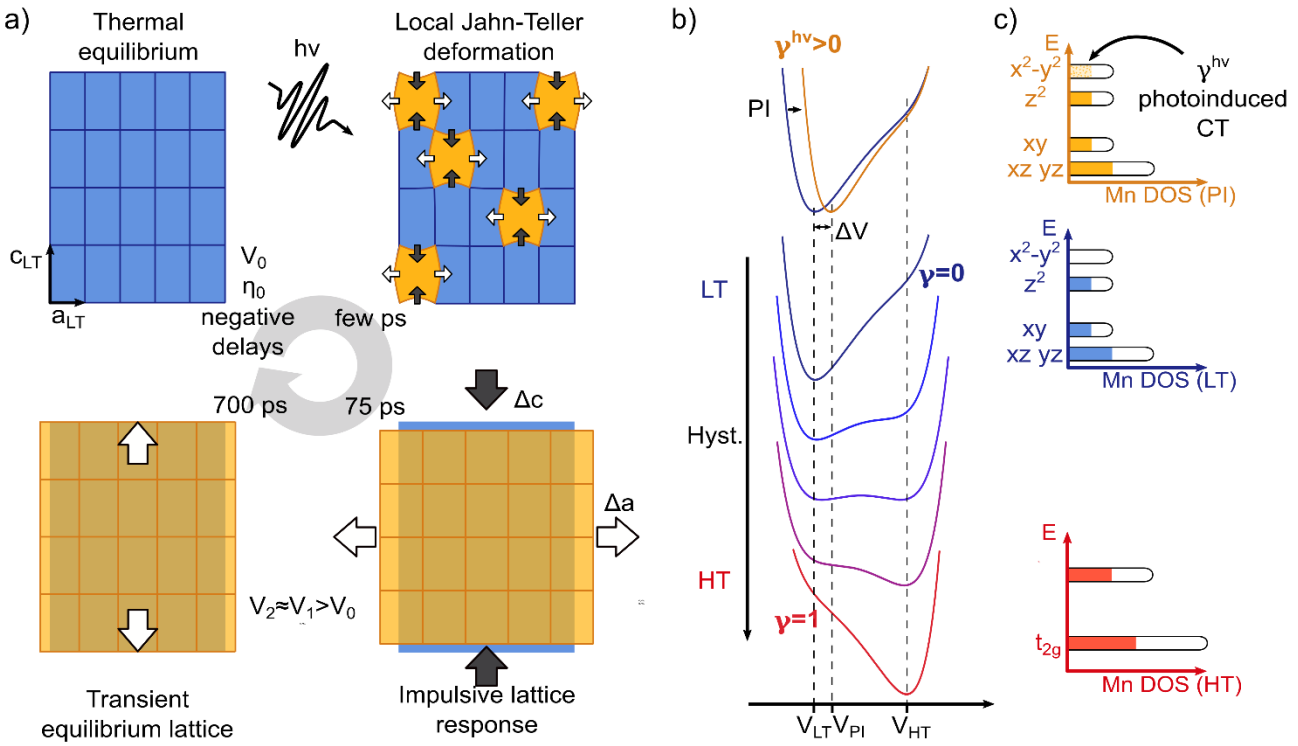

Figure 4: (a) Schematic representation of the structural changes caused by the photoexcitation with the local structural trapping, the dynamical expansion along a and contraction along c and the transient equilibrium lattice expended along a. (b) Schematic representation of the evolution of the lattice potential with different equilibrium volume during the thermal phase transition (bottom) and for a fraction $\gamma^{h\nu}$ of photo-induced CT state (top). The grey dotted lines mark the values of the Volume in the LT, HT and photo-induced (PI) phases.
(c) Schematic representation of the density of states in the HT, LT and PI states (bottom, middle, top). The colored parts schematically represent the occupation of each band in relation with Fig. 1b.

Acknowledgement
Parts of this research were carried out in the frame of the IM-LED LIA (CNRS) and a JSPS Grant-in-Aid for Scientific Research (A) 20H00369 and JSPS KAKENHI 16H06521 Co-ordination Asymmetry. The authors gratefully acknowledge Agence Nationale de la Recherche for financial support undergrant ANR-16-CE30-0018, ANR-19-CE30-0004, ANR-19-CE07-0027, the University Rennes 1 and the Fondation Rennes 1 for funding.

Supplementary Information

Samples preparation

We used microcrystals of $Rb_{0.94}Mn[Fe(CN)_6]_{0.98}\bullet 2.5H_2O$ synthesized by mixing a polyethylene glycol monolaurate (PEGM) matrix containing $MnCl_2$ (aq) and RbCl (aq) with another PEGM matrix containing $K_3[Fe(CN)_6]$ (aq) and RbCl (aq). The obtained precipitate was centrifuged, washed in methanol and dried in air as described in ref [23]. The chemical formula was confirmed using elemental analysis and infrared spectroscopy. The sample we used is a dispersion of microcrystals in ethanol (Fig.S1a) that was deposited on a glass substrate (Fig.S1b). The scanning electron microscope (SEM) images revealed that the crystals are plate-shaped and with good crystallinity (Fig. S1c). Fig. S2 shows the $\chi_M.T$ *vs* T (χ_M being the molar magnetic susceptibility and T the temperature).[23] The $\chi_M.T$ value (≈ 4.75 $cm^3.K.mol^{-1}$ at 300 K) of the HT phase $Fe^{III}(S=1/2)Mn^{II}(S=5/2)$ decreases around $T_{1/2\downarrow}\approx$ 185 K on cooling, as the LT phase $Fe^{II}(S=0)Mn^{III}(S=2)$ forms. Conversely, on warming the sample from the LT phase, the $\chi_M.T$ value increases around $T_{1/2\uparrow}\approx$ 285 K.

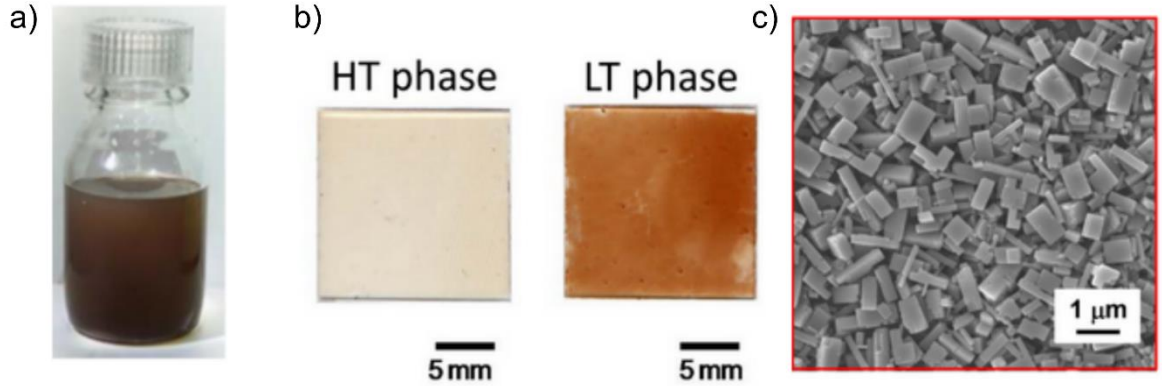

Fig. S1 $Rb_{0.94}Mn[Fe(CN)_6]_{0.98}\bullet 2.5H_2O$ sample in solution (a) and deposited on glass substrate changing color between the HT and LT phases (b). Sem image of the sample (c).

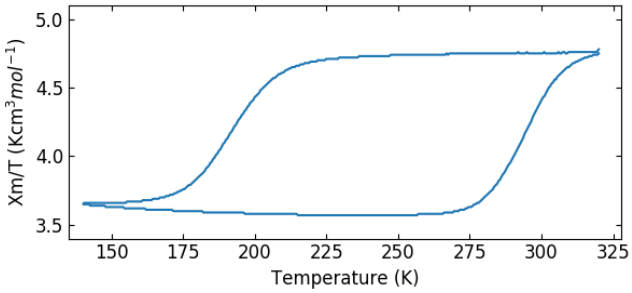

Fig. S2 – Thermal transition probed through the $\chi_M.T$ product (χ_M = molar magnetic susceptibility and T = temperature).

X-ray diffraction

The X-ray diffraction experiment was performed at the ID09 beamline of the ESRF synchrotron.[44] The beam was focused using a toroidal mirror and the beam size at the focal point was 150 x 150 μm^2. The footprint on the sample, due to the quasi-grazing angle experimental geometry was roughly 0.150 x 3 mm^2. We performed the measurements by keeping the sample surface close to grazing angle with respect to the X-rays incident direction. The energy of the beam was set to 14.8 keV by regulating the undulator gap. The samples were fixed to a goniometer head mounted on a Huber 1-Circle Goniometer (model 410a) with the rotation axis perpendicular both to the X-rays and laser directions. Temperature control during the experiment was achieved using an Oxford Cryosystems Cryostream 800 liquid nitrogen cooler positioned along the rotation axis of the goniometer. The thermal scans were performed using a cooling/heating rate of 6 K/min.

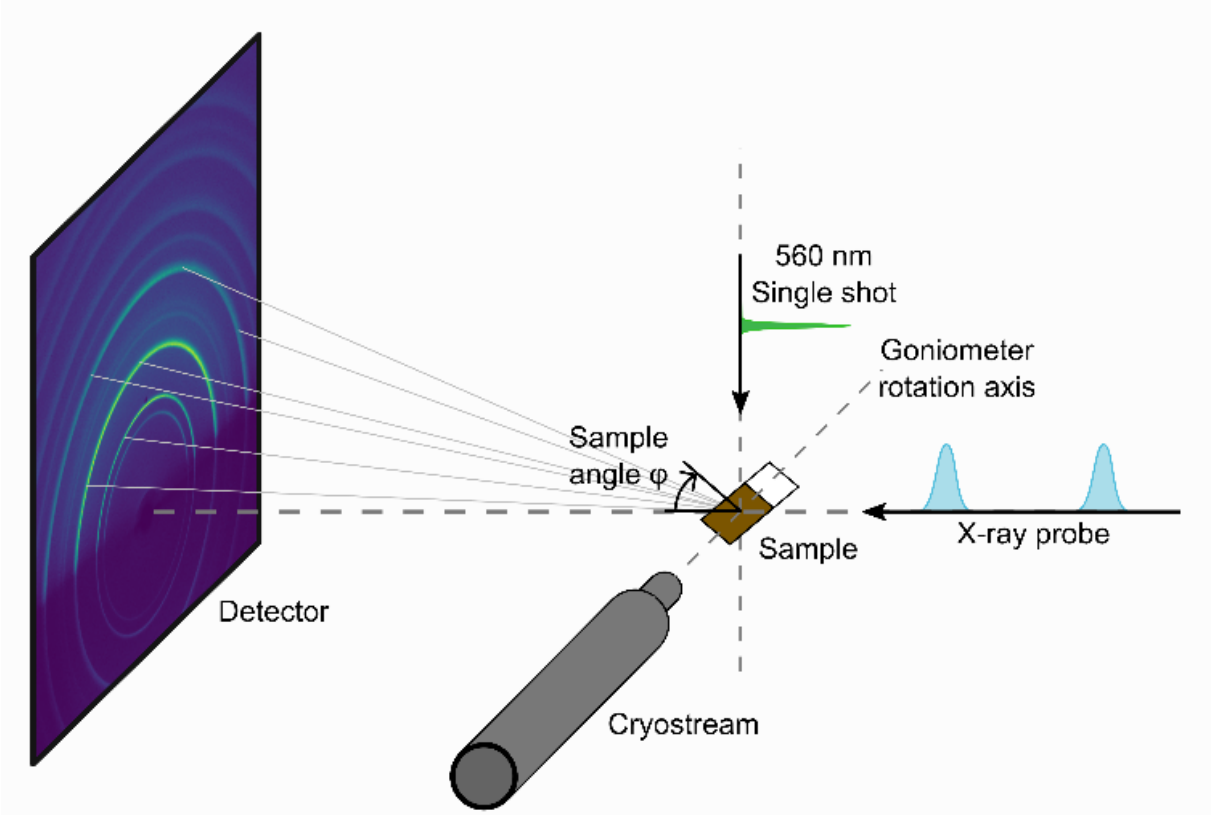

Fig. S3 - Schematic representation of the experimental setup used for the time-resolved measurements at ID09.

We collected the X-ray diffracted intensity with Rayonix MX170-HS CCD detector, with an active area of 170x170mm^2 and a pixel size of 89 µm. We chose a distance of ~23 cm from the sample as a trade-off between ***q***-resolution and portion of ***q***-space explored. A schematic representation of the setup geometry and a typical diffraction image are shown in Fig. S3. In order to increase the statistics, each image was collected using the integration of numerous X-ray shots. The diffraction data were refined using the software TOPAS-Academic version 6.[52] For monitoring the thermally-induced phase transition, we collected x-ray diffraction during a continuous thermal ramp, averaging the data collected within 10 K intervals. The almost zero thermal expansion showed by the MnFe system, revealed by high resolution diffraction studies[23] could not be accurately monitored by our experimental set-up, due to the relatively poor ***q***-resolution. The refinement process had to take into account the presence of crystals of a known and passive $Rb_2Mn[Fe(CN)_6]\bullet 3.5H_2O$ impurity. The temperature dependance of the lattice parameters of the $Rb_{0.94}Mn[Fe(CN)_6]_{0.98}\bullet 2.5H_2O$ sample shown in Fig. 2 exhibits a phase transition around 280 K on warming, in good agreement with the magnetic susceptibility (Fig. S2).

In order to study the out-of-equilibrium dynamics, we used a regenerative amplifier coupled to an OPA in order to generate ~1 ps pulses centered around 520 nm (Fig. S3). This wavelength is shown to efficiently promote the intervalence charge transfer from $Mn^{III}Fe^{II}$ to $Mn^{II}Fe^{III}$ using both continuous[43] and pulsed[46] irradiation. The penetration depth in RbMnFe can be calculated starting from the values of the real and imaginary parts of the dielectric constant reported in ref[29] and the penetration depth at 520 nm is around 320 nm, which is similar to the 300 nm average size of the microcrystals composing the sample. This ensures a rather homogeneous excitation at the individual microcrystal scale. We used a quasi-grazing incidence geometry with the sample surface tilted around 4° with respect to the X-ray direction and a laser incidence perpendicular to the direction of the film (Fig. S3). This allows for increasing the diffracted signal from the thin film of microcrystals by maximizing the excited area of the sample. This geometry is used to compensate the relatively low X-ray flux, due to the chopper system for time-resolved measurements in use at ID09 for time resolved measurements.[44]

The optical pump – X-ray probe experiment was performed with ~70 ps time resolution ($\sigma \simeq 30\,ps$), at a repetition rate of 1 kHz. The time resolution of the experiment was limited by the X-ray pulse duration. The time delay between the pump and the probe was controlled electronically. Each diffraction pattern was collected by integrating the diffracted intensity of up to 3000 X-ray shots at a given time delay. The negative delay signal (-10 ns) was used as reference and was collected several times during each scan to check the complete relaxation of the sample. We used excitation fluences up to 42 µJ.mm^{-2}. Higher fluences may have resulted in photo-induced residual effects indicating an incomplete relaxation of the sample that would make the data interpretation inconclusive. We collected data at several temperatures (110 K, 130 K and 160 K) outside the bistability region to allow for complete relaxation of the sample.

Fig. S4 shows an example of a time-resolved (top) X-ray diffraction pattern I(***q***) collected 10 ns before laser excitation (negative delays). The bottom pannel shows the differences between the intensity measured at postive delays and the reference signal at negative delay. The diffraction patterns were obtained by azimuthal integration of the diffracted intensity images using the python library PyFAI.[53] Due to the limitation given by the experimental geometry, the presence of the impurity in the sample and the small intensity of the photoinduced signal, it was not possible to perform a Rietveld refinement on the data. We used a Pawley refinement to retrieve the value of the lattice parameters as function of the time delay, using the software TOPAS-Academic version 6.[52] The data at negative delays were refined using the tetragonal LT phase and the cubic impurity. The experimental parameters were refined using these data and were kept fixed during the rest of the analysis.

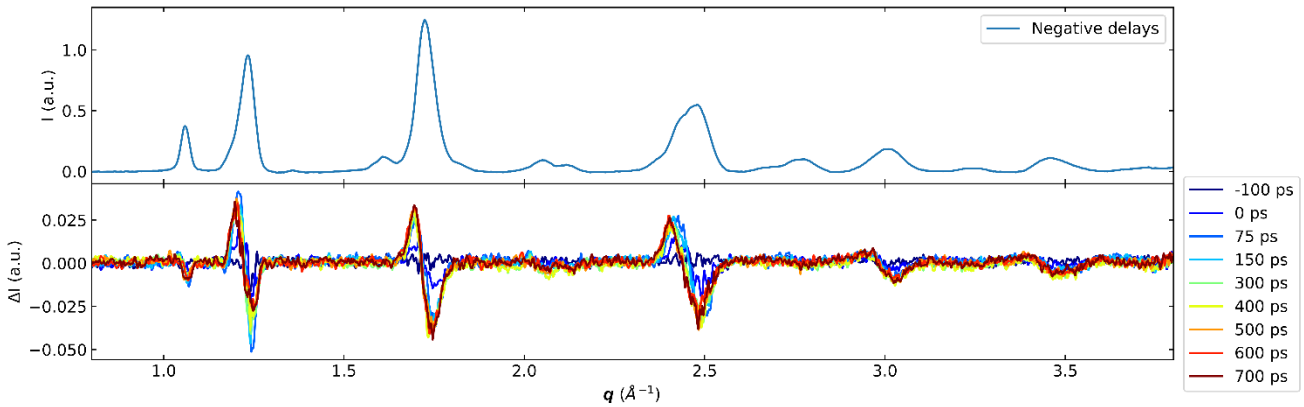

Fig. S4 - Diffraction patterns measured 10 ns before laser excitation (negative delays top) and difference signal for different time delays (bottom)

The data presented in Figure 3 were obtained by allowing volume expansion of the passive $Rb_2Mn[Fe(CN)_6]\bullet 3.5H_2O$ impurity. These cubic crystals exhibits a weak thermal expansion but does not undergo volume-changing charge-transfer transition. For checking the contribution of this impurity in the conclusion of our work on the lattice dynamics of photoexcited $Rb_{0.94}Mn[Fe(CN)_6]_{0.98}\bullet 2.5H_2O$ crystals, we compare in Fig. S5 the results of the Pawley analysis taking into account the lattice expansion of the impurity (***a***$_{imp}$) or not. In both cases we observe for the photoactive $Rb_{0.94}Mn[Fe(CN)_6]_{0.98}\bullet 2.5H_2O$ crystals the same qualitative response with an initial opposite shift of the lattice parameters ***a*** and ***c*** (clearly seen in the differential data by the opposite shift of the (h00) and (00l) peaks of the $Rb_{0.94}Mn[Fe(CN)_6]_{0.98}\bullet 2.5H_2O$ sample shown in Fig. 2). These shifts decrease the symmetry breaking order parameter η and result in a global volume expansion. Both analysis shown in Fig. S5 underline the out-of-equilibrium decoupling in time of the volume strain and the ferroelastic distortion.

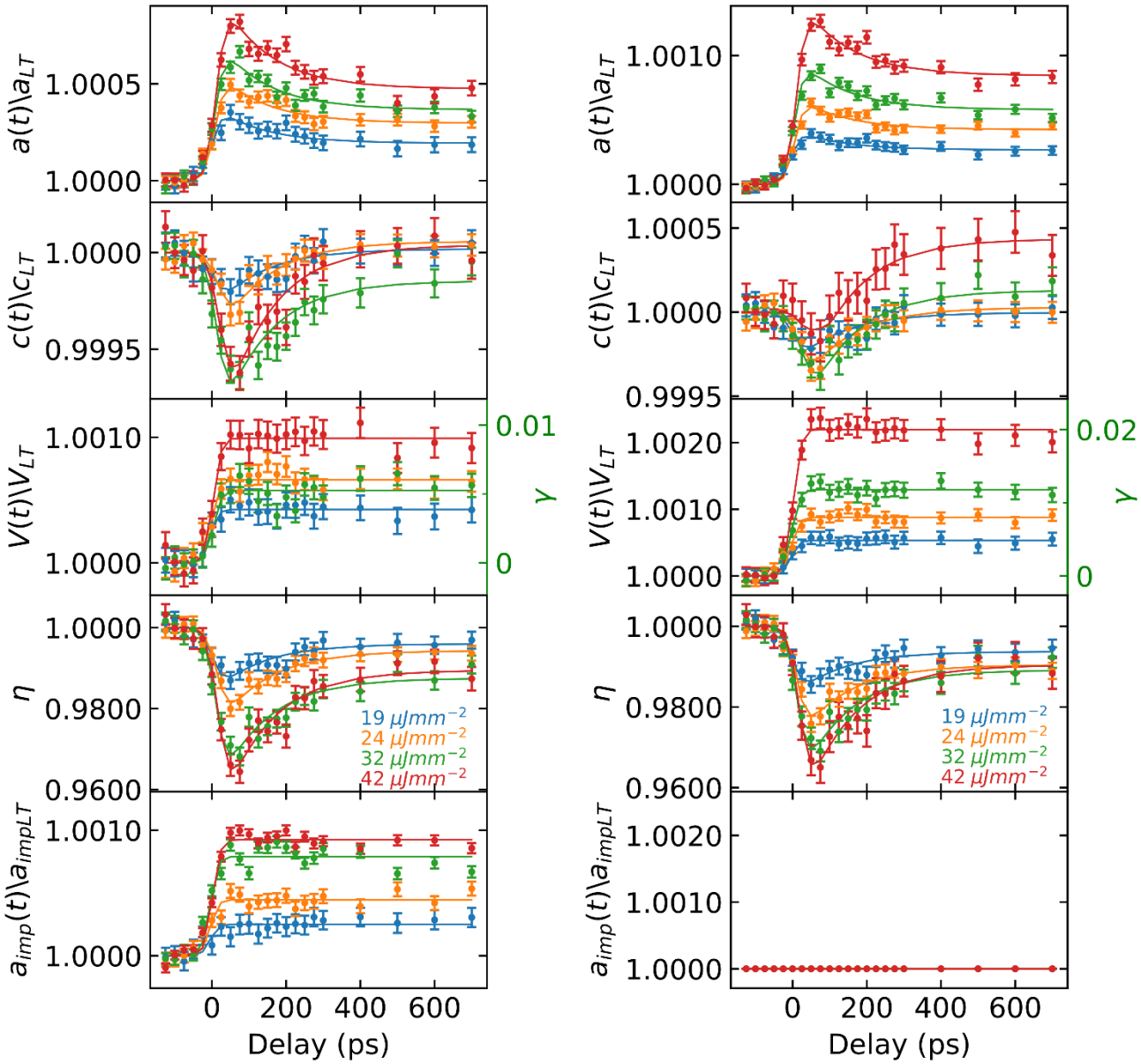

Fig. S5 - Relative temporal evolution at 130 K and for different laser fluences of the lattice parameters a, c, V and η of the $Rb_{0.94}Mn[Fe(CN)_6]_{0.98}$•$2.5H_2O$ photoactive crystals, with respect to values prior to photoexcitation. The figure on the left corresponds to the Pawley analysis allowing a thermal expansion of the cubic crystals (a_{imp}) of the passive $Rb_2Mn[Fe(CN)_6]$•$3.5H_2O$ impurity. The figure on the right corresponds to the Pawley analysis without change of the lattice impurity (a_{imp} fixed). Both analysis provide similar qualitative features for the time dependence of V and η, which are the key lattice parameters describing the phase transition.

The fits of the time dependent volume $\frac{V(t)}{V_{LT}}$ in Fig. 3 and S5 were performed using a convolution of a Gaussian Instrumental Response Function (IRF) with a step function $H(t)$: $\frac{V(t)}{V_{LT}} = IRF(t) \otimes [A.H(t)]$. A is the amplitude of the step and the $IRF(t) = \frac{1}{\sqrt{2\pi}\sigma} \exp(-\frac{t^2}{2\sigma^2})$ is characterized by $\sigma \simeq 30\ ps$ corresponding to an overall time resolution of ~70 ps. For the fits of the time-dependent signals $s(t)$ of the others lattice parameters, we add an exponential component; $s(t) = IRF_X(t) \otimes \left[\left(A - B \exp\left(\frac{-t}{\tau_r}\right)\right) * H(t)\right]$. τ_r ≃130 ps provides a satisfactory guide for the eye. Fig. S6 shows the effect of the limited time resolution on the signal. Fig. S7 shows the almost linear response with excitation density of the photoinduced lattice changes $\Delta \boldsymbol{a}^{h\upsilon}$, $\Delta \boldsymbol{c}^{h\upsilon}$ and $\Delta \boldsymbol{V}^{h\upsilon}$ fitted at 75 ps.

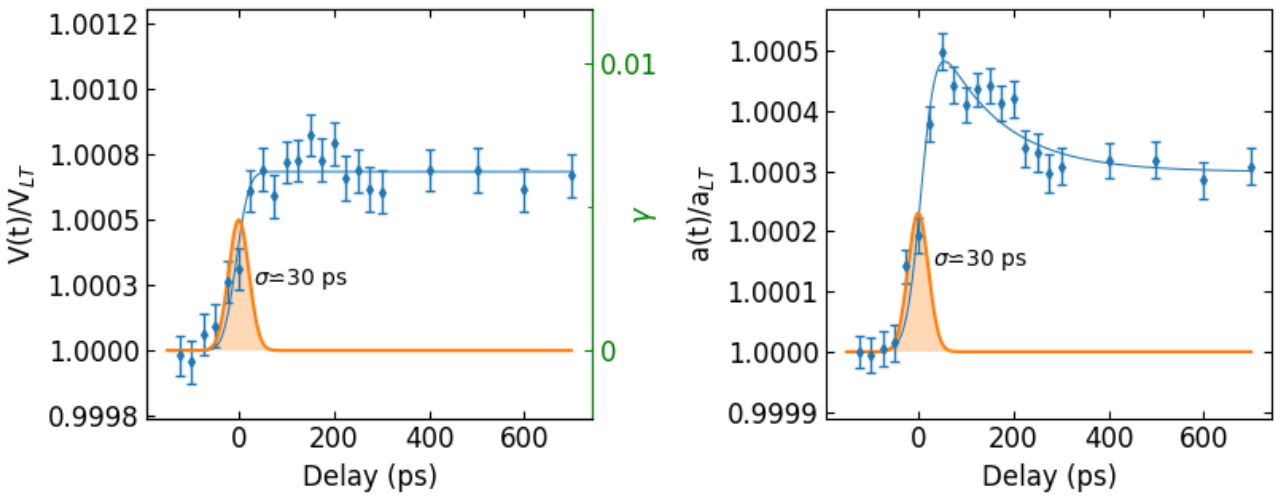

Fig. S6 – Fit of the temporal dependence of $\frac{V(t)}{V_{LT}}$ (left) and $\frac{\boldsymbol{a}(t)}{\boldsymbol{a}_{LT}}$ (right). The volume variation $\Delta V^{h\upsilon}$ as function of the pump fluence is scaled to the fraction γ of CT state (green right axis).

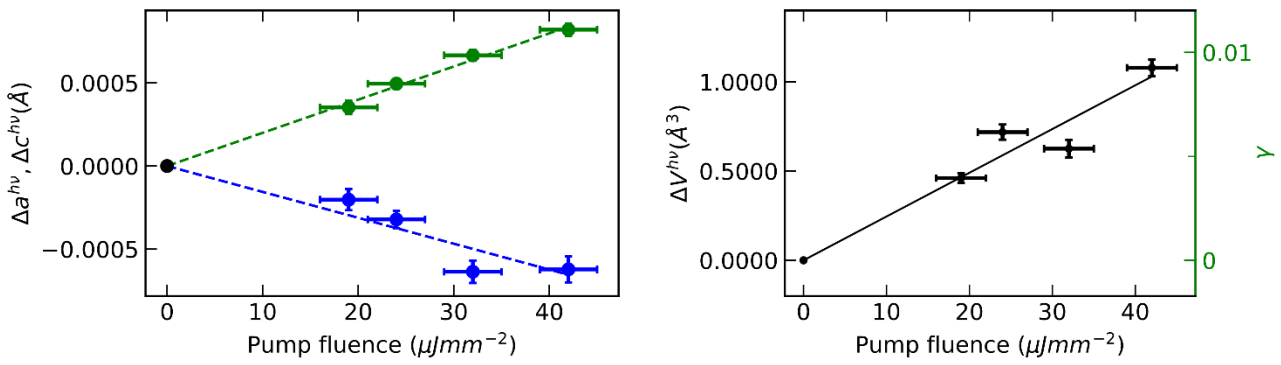

Fig. S7 – Evolution of the photoinduced shift of lattice parameters $\Delta \boldsymbol{a}^{h\upsilon}$ and $\Delta \boldsymbol{c}^{h\upsilon}$ (left) and volume expansion $\Delta V^{h\upsilon}$ (right) as function of the pump fluence. The volume change is scaled to γ (green right axis).

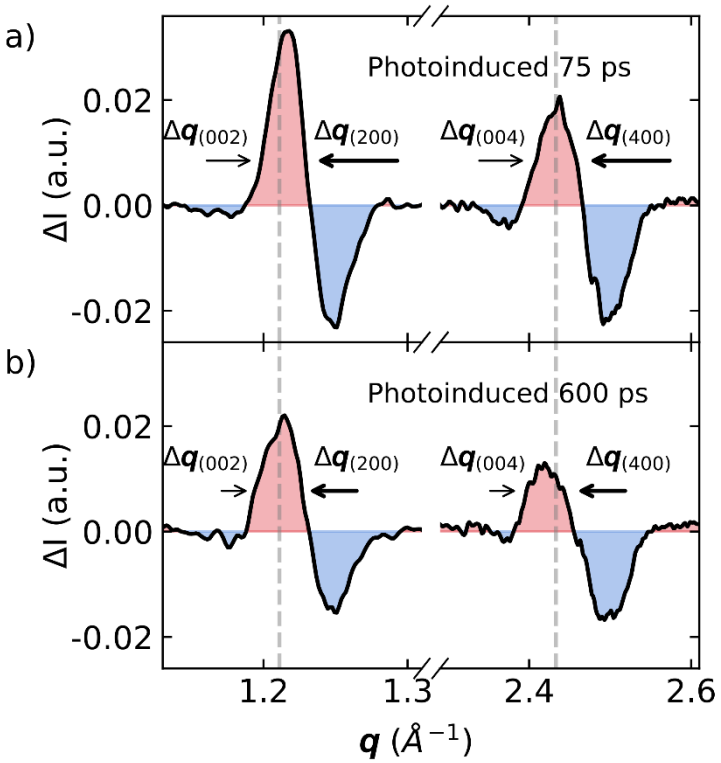

*Fig. S8 Evolution of the time-resolved differential X-ray diffraction signal, with respect to negative delay, measured 75 ps and 600 ps after photoexcitation. The contribution of the lattice contraction along **c** is stronger at 75 ps than at 600 ps, where it is mainly the lattice expansion along **a** that contributes to the signal change.*

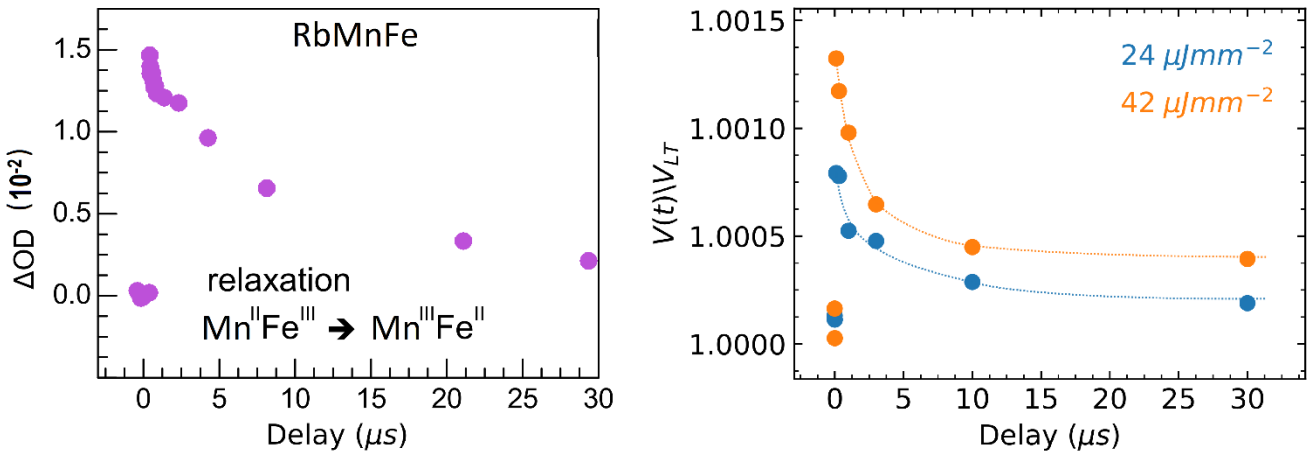

Fig. S9 Optical density change (ΔOD) probed at 650 nm for the RbMnFe compound after fs laser excitation at 530 nm, monitoring the decay of the photoinduced $Mn^{III}Fe^{II}$ state (left, reprinted with permission from ref [45]). The volume probed by time-resolved X-ray diffraction and the photoinduced CT states decay within 10s μs.

References

1. D. N. Basov, R. D. Averitt and D. Hsieh, Nature Materials **16**, 1077 (2017).
2. M. Liu, H. Y. Hwang, H. Tao, A. C. Strikwerda, K. Fan, G. R. Keiser, A. J. Sternbach, K. G. West, S. Kittiwatanakul, J. Lu, S. A. Wolf, F. G. Omenetto, X. Zhang, K. A. Nelson and R. D. Averitt, Nature **487** (7407), 345-348 (2012).
3. T. Kampfrath, K. Tanaka and K. A. Nelson, Nature Photonics **7** (9), 680-690 (2013).
4. T. Ishikawa, S. A. Hayes, S. Keskin, G. Corthey, M. Hada, K. Pichugin, A. Marx, J. Hirscht, K. Shionuma, K. Onda, Y. Okimoto, S.-y. Koshihara, T. Yamamoto, H. Cui, M. Nomura, Y. Oshima, M. Abdel-Jawad, R. Kato and R. J. D. Miller, Science **350** (6267), 1501-1505 (2015).
5. K. Sokolowski-Tinten, C. Blome, J. Blums, A. Cavalleri, C. Dietrich, A. Tarasevitch, I. Uschmann, E. Forster, M. Kammler, M. Horn-von-Hoegen and D. von der Linde, Nature **422** (6929), 287-289 (2003).
6. D. M. Fritz, D. A. Reis, B. Adams, R. A. Akre, J. Arthur, C. Blome, P. H. Bucksbaum, A. L. Cavalieri, S. Engemann, S. Fahy, R. W. Falcone, P. H. Fuoss, K. J. Gaffney, M. J. George, J. Hajdu, M. P. Hertlein, P. B. Hillyard, M. H. V. Hoegen, M. Kammler, J. Kaspar, R. Kienberger, P. Krejcik, S. H. Lee, A. M. Lindenberg, B. McFarland, D. Meyer, T. Montagne, E. D. Murray, A. J. Nelson, M. Nicoul, R. Pahl, J. Rudati, H. Schlarb, D. P. Siddons, K. Sokolowski-Tinten, T. Tschentscher, D. von der Linde and J. B. Hastings, Science **315** (5812), 633-636 (2007).
7. L. Rettig, S. O. Mariager, A. Ferrer, S. Grübel, J. A. Johnson, J. Rittmann, T. Wolf, S. L. Johnson, G. Ingold, P. Beaud and U. Staub, Structural Dynamics **3** (2), 023611 (2016).
8. R. Bertoni, M. Lorenc, H. Cailleau, A. Tissot, J. Laisney, M. L. Boillot, L. Stoleriu, A. Stancu, C. Enachescu and E. Collet, Nat Mater **15** (6), 606-610 (2016).
9. M. Lorenc, J. Hebert, N. Moisan, E. Trzop, M. Servol, M. Buron-Le Cointe, H. Cailleau, M. L. Boillot, E. Pontecorvo, M. Wulff, S. Koshihara and E. Collet, Physical Review Letters **103** (2), - (2009).
10. F. X. Morrissey and S. L. Dexheimer, Physical Review B **81** (9), 094302 (2010).
11. A. Mishima and K. Nasu, Physical Review B **39** (9), 5758-5762 (1989).
12. Y. Toyozawa, Progress of Theoretical Physics **26** (1), 29-44 (1961).
13. S. Li, J. Luo, J. Liu and J. Tang, The Journal of Physical Chemistry Letters **10** (8), 1999-2007 (2019).
14. S. Ismail-Beigi and S. G. Louie, Physical Review Letters **95** (15), - (2005).
15. S. L. Dexheimer, A. D. Van Pelt, J. A. Brozik and B. I. Swanson, Physical Review Letters **84** (19), 4425-4428 (2000).
16. M. Matus, H. Kuzmany and E. Sohmen, Physical Review Letters **68** (18), 2822-2825 (1992).
17. S. Ohkoshi, K. Imoto, Y. Tsunobuchi, S. Takano and H. Tokoro, Nature Chemistry **3** (7), 564-569 (2011).
18. S. Ohkoshi, S. Takano, K. Imoto, M. Yoshikiyo, A. Namai and H. Tokoro, Nat Photon **8** (1), 65-71 (2014).
19. H. Tokoro, T. Matsuda, T. Nuida, Y. Moritomo, K. Ohoyama, E. D. L. Dangui, K. Boukheddaden and S. Ohkoshi, Chem Mater **20** (2), 423-428 (2008).
20. M. Verdaguer, A. Bleuzen, V. Marvaud, J. Vaissermann, M. Seuleiman, C. Desplanches, A. Scuiller, C. Train, R. Garde, G. Gelly, C. Lomenech, I. Rosenman, P. Veillet, C. Cartier and F. Villain, Coordination Chemistry Reviews **190–192**, 1023-1047 (1999).
21. D. Aguila, Y. Prado, E. S. Koumousi, C. Mathoniere and R. Clerac, Chemical Society Reviews **45** (1), 203-224 (2016).
22. M. Cammarata, S. Zerdane, L. Balducci, G. Azzolina, S. Mazerat, C. Exertier, M. Trabuco, M. Levantino, R. Alonso-Mori, J. M. Glownia, S. Song, L. Catala, T. Mallah, S. F. Matar and E. Collet, Nature Chemistry **13** (1), 10-14 (2021).
23. H. Tokoro, K. Nakagawa, K. Imoto, F. Hakoe and S. Ohkoshi, Chem Mater **24** (7), 1324-1330 (2012).
24. A. Bleuzen, J.-D. Cafun, A. Bachschmidt, M. Verdaguer, P. Münsch, F. Baudelet and J.-P. Itié, The Journal of Physical Chemistry C **112** (45), 17709-17715 (2008).
25. L. Trinh, S. Zerdane, S. Mazérat, N. Dia, D. Dragoe, C. Herrero, E. Rivière, L. Catala, M. Cammarata, E. Collet and T. Mallah, Inorganic Chemistry **59** (18), 13153-13161 (2020).
26. G. Molnár, S. Cobo, T. Mahfoud, E. J. M. Vertelman, P. J. van Koningsbruggen, P. Demont and A. Bousseksou, The Journal of Physical Chemistry C **113** (6), 2586-2593 (2009).
27. G. Azzolina, E. Collet, C. Mariette, M. Cammarata, E. Trzop, M. Sander, M. Levantino, K. Nakagawa, H. Tokoro, S. Ohkoshi and R. Bertoni, Eur J Inorg Chem **2019** (27), 3142-3147 (2019).
28. S. Ohkoshi and H. Tokoro, Accounts of Chemical Research **45** (10), 1749-1758 (2012).

29. S. Ohkoshi, T. Nuida, T. Matsuda, H. Tokoro and K. Hashimoto, Journal of Materials Chemistry **15** (32), 3291 (2005).
30. G. Azzolina, R. Bertoni, C. Ecolivet, H. Tokoro, S. Ohkoshi and E. Collet, Physical Review B **102** (13), 134104 (2020).
31. P. Beaud, A. Caviezel, S. O. Mariager, L. Rettig, G. Ingold, C. Dornes, S. W. Huang, J. A. Johnson, M. Radovic, T. Huber, T. Kubacka, A. Ferrer, H. T. Lemke, M. Chollet, D. Zhu, J. M. Glownia, M. Sikorski, A. Robert, H. Wadati, M. Nakamura, M. Kawasaki, Y. Tokura, S. L. Johnson and U. Staub, Nat Mater **13** (10), 923-927 (2014).
32. E. Collet, M. H. Lemee-Cailleau, M. Buron-Le Cointe, H. Cailleau, M. Wulff, T. Luty, S. Y. Koshihara, M. Meyer, L. Toupet, P. Rabiller and S. Techert, Science **300** (5619), 612-615 (2003).
33. H. Tokoro, S. Ohkoshi and K. Hashimoto, Applied Physics Letters **82** (8), 1245-1247 (2003).
34. H. Tokoro, S. Ohkoshi, T. Matsuda and K. Hashimoto, Inorganic Chemistry **43** (17), 5231-5236 (2004).
35. H. Tokoro, A. Namai, M. Yoshikiyo, R. Fujiwara, K. Chiba and S. Ohkoshi, Sci Rep **8** (1), 63 (2018).
36. C. Cartier dit Moulin, F. Villain, A. Bleuzen, M.-A. Arrio, P. Sainctavit, C. Lomenech, V. Escax, F. Baudelet, E. Dartyge, J.-J. Gallet and M. Verdaguer, Journal of the American Chemical Society **122** (28), 6653-6658 (2000).
37. G. Azzolina, E. Collet, C. Mariette, M. Cammarata, E. Trzop, M. Sander, M. Levantino, K. Nakagawa, H. Tokoro, S.-i. Ohkoshi and R. Bertoni, Eur J Inorg Chem **2019** (27), 3142-3147 (2019).
38. Y. Moritomo, K. Kato, A. Kuriki, M. Takata, M. Sakata, H. Tokoro, S. Ohkoshi and K. Hashimoto, Journal of the Physical Society of Japan **71** (9), 2078-2081 (2002).
39. H. Tokoro, K. Hashimoto and S. Ohkoshi, J Magn Magn Mater **310** (2), 1422-1428 (2007).
40. H. Tokoro, S. Miyashita, K. Hashimoto and S. Ohkoshi, Physical Review B **73**, 172415 (2006).
41. S. Ohkoshi, H. Tokoro, M. Utsunomiya, M. Mizuno, M. Abe and K. Hashimoto, The Journal of Physical Chemistry B **106** (10), 2423-2425 (2002).
42. K. Kato, Y. Moritomo, M. Takata, M. Sakata, M. Umekawa, N. Hamada, S. Ohkoshi, H. Tokoro and K. Hashimoto, Physical Review Letters **91**, 255502 (2003).
43. S. Ohkoshi, T. Matsuda, H. Tokoro and K. Hashimoto, Chem Mater **17** (1), 81-84 (2005).
44. M. Cammarata, L. Eybert, F. Ewald, W. Reichenbach, M. Wulff, P. Anfinrud, F. Schotte, A. Plech, Q. Kong, M. Lorenc, B. Lindenau, J. Rabiger and S. Polachowski, Rev Sci Instrum **80** (1), 015101 (2009).
45. S. Zerdane, M. Cammarata, L. Balducci, R. Bertoni, L. Catala, S. Mazerat, T. Mallah, M. N. Pedersen, M. Wulff, K. Nakagawa, H. Tokoro, S. Ohkoshi and E. Collet, Eur J Inorg Chem **2018** (3-4), 272-277 (2018).
46. A. Asahara, M. Nakajima, R. Fukaya, H. Tokoro, S. Ohkoshi and T. Suemoto, Physical Review B **86** (19) (2012).
47. S. Koshihara, Y. Takahashi, H. Sakai, Y. Tokura and T. Luty, The Journal of Physical Chemistry B **103** (14), 2592-2600 (1999).
48. S. Wall, S. Yang, L. Vidas, M. Chollet, J. M. Glownia, M. Kozina, T. Katayama, T. Henighan, M. Jiang, T. A. Miller, D. A. Reis, L. A. Boatner, O. Delaire and M. Trigo, Science **362** (6414), 572-576 (2018).
49. K. Boukheddaden, E. D. Loutete-Dangui, E. Codjovi, M. Castro, J. A. Rodriguéz-Velamazán, S. Ohkoshi, H. Tokoro, M. Koubaa, Y. Abid and F. Varret, Journal of Applied Physics **109** (1), 013520 (2011).
50. F. S. Krasniqi, S. L. Johnson, P. Beaud, M. Kaiser, D. Grolimund and G. Ingold, Physical Review B **78** (17) (2008).
51. H. Spiering, K. Boukheddaden, J. Linares and F. Varret, Physical Review B **70**, 184106 (2004).
52. A. Coelho, Journal of Applied Crystallography **51** (1), 210-218 (2018).
53. G. Ashiotis, A. Deschildre, Z. Nawaz, J. P. Wright, D. Karkoulis, F. E. Picca and J. Kieffer, Journal of Applied Crystallography **48** (2), 510-519 (2015).